4D spatiotemporal evolution of liquid spray using kHz-rate x-ray computed tomography

B. R. Halls,[1,2]* N. Rahman,[3] M.N. Slipchenko,[3,4] J. W. James,[3,5] A. McMaster,[1,5] M. D. A. Ligthfoot,[6] J. R. Gord,[2] and T. R. Meyer[3]

[1]Engineering Sciences Center, Sandia National Laboratories, Albuquerque, NM
[2]Air Force Research Laboratory, Aerospace Systems Directorate, Wright-Patterson Air Force Base, OH 45433 USA
[3]Purdue University, School of Mechanical Engineering, West Lafayette, IN 47907 USA
[4]Spectral Energies, LLC, Beavercreek, OH 45430 USA
[5]Fort Lewis College, Department of Physics and Engineering, Durango, CO 8130 USA
[6]Air Force Research Laboratory, Aerospace Systems Directorate, Edwards Air Force Base, CA 93524 USA

*Corresponding author: brhalls@sandia.gov

Received XX Month XXXX; revised XX Month, XXXX; accepted XX Month XXXX; posted XX Month XXXX (Doc. ID XXXXX); published XX Month XXXX

Four-dimensional (x, y, z, t) x-ray computed tomography was demonstrated in an optically complex spray using an imaging system consisting of three x-ray sources and three high-speed detectors. The x-ray sources consisted of high-flux rotating anode x-ray tube sources that illuminated the spray from three lines of sight. The absorption along each absorption path was collected using a CsI phosphor plate and imaged by a high-speed intensified CMOS camera at 20 kHz. The radiographs were converted to a quantitative equivalent path length (EPL) of liquid using a variable attenuation coefficient to account for beam hardening. The EPL data were then reconstructed using the algebraic reconstruction technique into high-speed time sequences of the three-dimensional liquid mass distribution.

OCIS codes: *(110.6955) Tomographic imaging; (110.6880) Three-dimensional image acquisition; (110.7440) X-ray imaging.*

http://dx.doi.org/10.1364/OL.99.099999

Spray breakup and atomization are integral parts of many chemical processes and applications. In devices used for power generation and propulsion, for example, the spray and reacting environment are closely coupled and affect the stability, performance, and emissions of the combustion system [1,2]. Knowledge of the time-evolving, three-dimensional (3D) liquid distribution near the injector tip, therefore, is important for optimizing downstream fuel-air mixing processes in a wide range of practical devices. This requires a technique that can interrogate the dense region of the spray and resolve the 3D (x, y, z) flowfield in time (t).

Traditional optical measurements in the near field region of liquid injectors are challenging because ultraviolet-visible radiation is susceptible to refraction and multiple scattering events from liquid–gas interfaces [3,4]. A number of dense spray diagnostics have been developed and are summarized by Linne (2012).[5] The only current diagnostic capable of quantitative mass distribution measurements in optically complex sprays is through the use of x-ray radiation [5].

X-ray diagnostics have been applied for investigation of multiphase flows using both synchrotron sources, as discussed by Kastengren and Powell (2014) [6], and tube sources, as reviewed by Heindel (2011) [7]. Tube source measurements have been shown to yield time-averaged 3D images [2,8–10] and time-resolved 2D images [11–15]. Tube source measurements were shown to be quantitative by either narrowing the polychromatic spectrum by filtering the low energy x-rays [8], or by accounting for the broadband emission by modeling the imaging system and using a variable attenuation coefficient to account for beam hardening. [14,15]

Optical approaches have also been explored for three-dimensional measurements, including holography [16], shadowgraphy [17], structured illumination [18], and light-field imaging [19]. While these methods are capable of 3D measurements, they are limited in optically complex regions of the spray where large, intact liquid structures are present [5].

The current work examines the application of high-speed x-ray computed tomography using simultaneous radiography from multiple directions. This differs from approaches that require the x-ray source or the spray to be rotated over a relatively long duration that leads to a time-averaged map of the 3D liquid distribution, high-speed CT [20] or flash x-ray tomography which is limited only a few frames [21, 22]. Unfortunately, this limits the spatial and temporal information that can be gained and cannot be used to resolve dynamic features of the spray. The current approach results in a 3D image that can be collected within microseconds rather than minutes. It is an extension of laser-based tomographic measurements of continuously varying scalar fields using

techniques such as laser-induced incandescence [23] and laser-induced fluorescence [24], which require 5 or more views for accurate reconstructions. However, the presence of discrete features, such as particles in the case of tomographic PIV, can allow for a reduction in the number of views required [25]. Previous tomographic spray measurements have included shadowgraphy [17, 18, 26] and preliminary results of x-ray tomography [27]. Hence, the discrete, nearly binary nature of non-evaporating sprays existing as either liquid or gas provides an opportunity to achieve high-speed 4D (x, y, z, t) measurements of the liquid mass distribution.

The tomographic x-ray imaging system comprised three radiography subsystems, each composed of an x-ray tube source and a scintillator lens coupled to a high-speed intensified CMOS camera. The high-flux, rotating anode tube sources had 0.6-mm-diameter focal spots and tungsten anodes, as described in in prior work on high-speed two-dimensional x-ray imaging [15]. The 50x50 mm^2, 150-μm thick cesium iodide scintillators absorbed the x-ray photons and produced visible-light images. The visible scintillator emission was reflected off 2 inch turning prisms and directed into 50 mm *f*/2 Nikon objectives that were mounted to high-speed, two-stage intensifiers (Lavision, HS-IRO) coupled to high-speed CMOS cameras (Photron, SA-Z). The frame rate of each system was 20 kHz with an intensifier gate of 49 μs. The gains varied between 60–64% to balance the signals in each view.

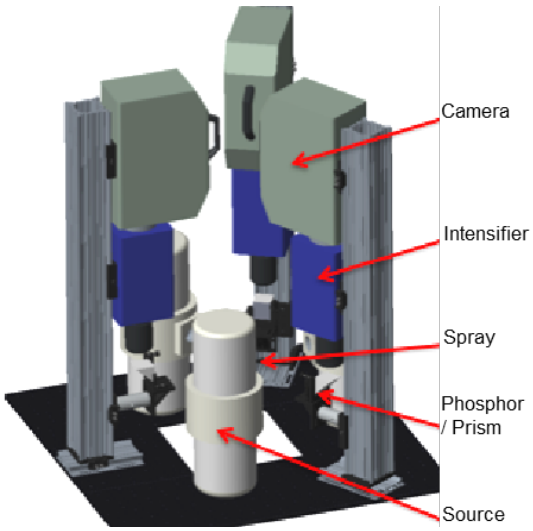

Fig. 1. Multiview imaging system composed of three x-ray tube sources and intensified imaging systems.

Image preprocessing was performed to account for the detector response function, normalize the data to the flat field, correct the source fluctuations, remove the background signal, correct for some of the spatial blur, convert transmission data to equivalent path length (EPL), and apply a threshold to achieve a zero background for tomographic reconstruction. The EPL represents the integrated liquid mass along each line of sight. Therefore, the mass distribution of was determined by: mass = liquid density × EPL × pixel area. The nonlinear detector response function was determined by varying the intensity of light incident upon the detector and measuring the signal intensity averaged across the entire image, and then corrected for. The flat field images were collected when no spray was present, and the normalization process corrected for the variation in the nonuniform illumination and in the signal response on a pixel-by-pixel basis. The image-to-image source fluctuations were sampled in a small region of the normalized images where no spray was present, and the mean signals in each image were set to unity. To reduce the probability of reconstruction artifacts in the 3D images, the images were flattened using smoothing and deconvolution. The images were temporally smoothed with a triangular filter that reduced the effective repetition rate to 10 kHz and spatially smoothed with a Gaussian filter (300 μm FWHM). The camera repetition rate was sufficiently fast to avoid temporal blurring, and the spatial resolution of ~1 mm in the final reconstructed volumes (discussed below) was not greatly affected by the spatial filtering. The blur was reduced using a Richardson-Lucy deconvolution algorithm. The deconvolution reduced the effect of the blur by ~50% using an experimentally derived point spread function determined by imaging a cylinder of known diameter. Due to the limited number of views, these processes did not appreciably change the spatial resolution in the final reconstructed volumes but help reduce reconstruction artifacts.

A complete description of the model and the calibration procedure to compute EPL for each image can be found in Halls et al. [15]. To briefly summarize, the source spectrum and scintillator response were modeled in Matlab using liquid-phase x-ray attenuation coefficients, scintillator absorption coefficients, and source spectra from the XOP database [28]. Softer (lower energy) x-rays in the polychromatic source spectrum are preferentially absorbed as they pass through the spray—an effect known as beam hardening—it is not feasible to determine the liquid-spray attenuation coefficient using a single path length. As such, x-ray attenuation coefficients were determined experimentally by measuring the attenuation through liquid jets of varying diameter. After the EPL was computed for each image, a threshold of 110 μm was set to achieve a zero background to reduce artifacts in the final reconstructed volumes.

The field of view per pixel was 30×30 μm^2 such that the spatial resolution of 320 μm in the images from each perspective view was limited by the penumbra from the x-ray source and blur in the detector systems rather than the pixel density. This resolution was determined by imaging a sharp edge and measuring the 10–90% rise distance. The attenuation-to-noise ratio of the images was ~10:1 based on the peak attenuation values and background noise.

The spray emanated from a 2-mm-diamter, solid cone injector with a 0.76 Lpm flow rate and 60-degree included angle. The injector was mounted above a large liquid catch that was centered between the sources and detectors. The liquid was water doped with potassium iodide (50% by mass) to increase x-ray attenuation and, therefore, the image contrast.

Time-series images of the spray at 10 kHz from the three perspective views are displayed in Fig. 2, with every fifth frame shown. The presented images show spray features convecting downstream at each successive time step, with each perspective showing a unique flow structure. The nearfield region is a contiguous liquid cone that begins to disintegrate into ligands and droplets as the flow propagates downstream. The liquid field spreads at an angle of 60 degrees, with some deviation in each view due to imperfections in the injector.

The two-dimensional EPL images with zero background were used to reconstruct three-dimensional volumes of liquid mass

fraction using a Multiplicative Algebraic Reconstruction Technique (MART) in commercially available LaVision Davis 8.3 software. The algorithm used an image-registration process that defined a common three-dimensional coordinate system. The registration process involved imaging an x-ray transparent dot target at several locations within the measurement volume. The coordinate system was determined to have sub-pixel accuracy, allowing for the volumetric information from the projections to overlap reliably in three-dimensional space since the image resolution of 320 μm was much larger than the pixel resolution of 30 μm.

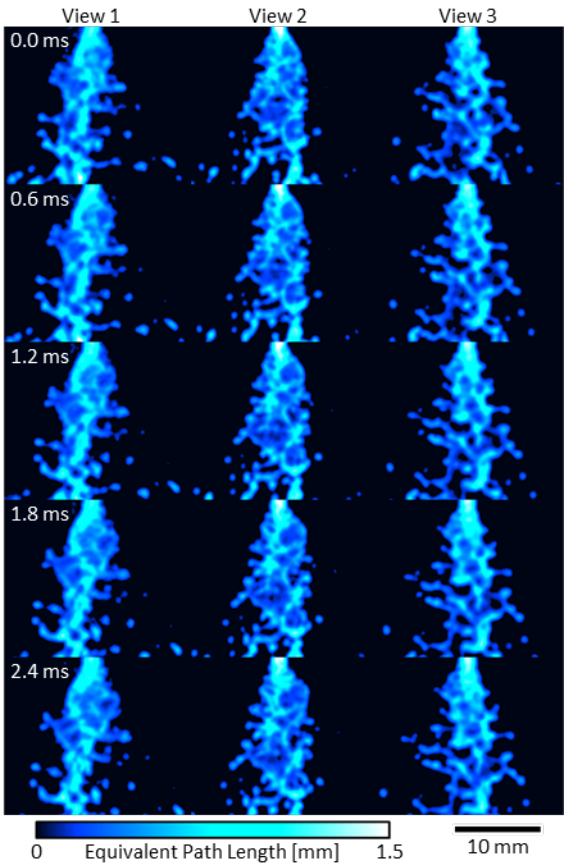

Fig. 2. Time sequences of EPL images of the solid cone spray from each of the three views used for reconstruction. Every fifth frame shown.

The MART reconstruction algorithm utilizes a set of under-determined linear equations in which the intensity of each voxel, or volume element, is related to the intensity of the corresponding pixels from each view. The reconstruction process involves 2 steps: 1) an initial volume guess using a back-projection method that smears the perspective information across the volume; and 2) an iterative process where projections of the guessed volume are compared to the perspective data and the corresponding voxels are updated and smoothed by a 3×3 triangular filter. The second step iterates until the convergence criterion is met, where the change in the volume data after each iteration reaches a constant value. The volume spatial resolution was estimated to be ~1 mm, dependent on the size and shape of the reconstructed object [29]. The reconstruction algorithm did not account for the cone beam from the tube source. The enclosed angle of the cone beam was 6.8 degrees based on the distance from the source and the width of the spray. This misplacement of mass degraded the spatial resolution by 0.3 mm. The resulting spatial resolution was estimated to be ~1 mm, based on the image resolution and losses in the reconstruction process. The signal-noise-ratio (SNR) was ~200:1 in the volumes. It is important to note that the SNR is not necessarily the measurement precision, which must consider the processing steps performed on the data from the normalized images to the final reconstructed volumes. The measurement uncertainty was limited by the calibration, spatial resolution, and reconstruction uncertainty. A sample set of the volumes is displayed in Fig. 3, where isocontours show the three-dimensional structure of the spray, and the series of images shows the evolution in time. Every sixth frame is shown to highlight the movement of larger structures. The information in the volumes is similar to that seen in the perspective data except that the information is now positioned properly in the measurement volume. The other notable change is the loss of spatial resolution due to the limited number of views and smoothing during the reconstructions process. This is an ongoing area of research attempting to acquire more and more information from limited numbers of views.

According to the isocountour plots in Fig. 3, the near field of the spray consists of an intact cone that begin to breakup two to four injector diameters below the injector. As this is a non-evaporating spray with a binary density distribution (either liquid or gas), it is feasible to reconstruct the liquid structures with only three perspective views because of their discrete nature. The regions that pose the greatest challenge to the reconstruction process have the most information that needs to be correctly placed in the three-dimensional space. In the spray shown here, this region is about four injector diameters downstream, where the spray is compact

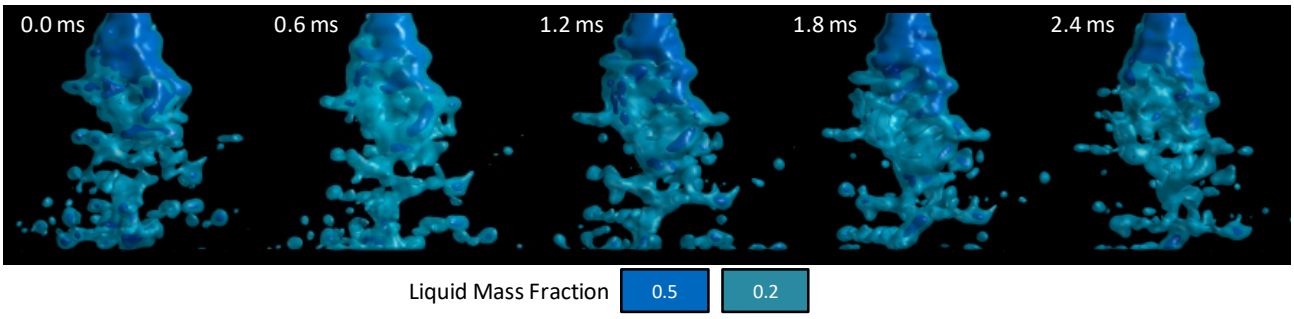

Fig. 3. Time-evolving, three-dimensional isocontours of liquid mass fraction of the solid cone spray, with every sixth volume shown.

but relatively complex. In this region, this can cause blurring of the liquid mass fraction values. As a result, the liquid structures shown in the 3D images display sub-unity mass fractions of the liquid phase within each voxel, as would be expected for any imaging technique that did not fully resolve the spatial structure.

These structures are visualized by taking a slice through the center plane of the spray, as shown in Fig. 4a, while the computed mass fractions are indicated by the line plots through that central slice, as shown in Fig. 4b. The liquid mass fraction values at the line plot 1.6 mm below the injector shows the value saturate at unity where the reconstruction is accurately determining the intact liquid structure. The line plots at 7.8 mm and 14.6 mm below the injector show sub-unity variations of the mixture fraction across the flow, likely due to unresolved flow structures such as ligands and droplets that are below the ~1 mm resolution of the 3D imaging system. These values are a function of the true mass fractions blurred by the imaging system and the reconstruction process. Nonetheless, the 3D images show complex liquid mass distribution as the liquid propagates downstream and undergoes primary and secondary breakup. As such, the behavior of the spray and the breakup dynamics represented by the evolution of the flow structure is captured and can be tracked in all three spatial dimensions and time.

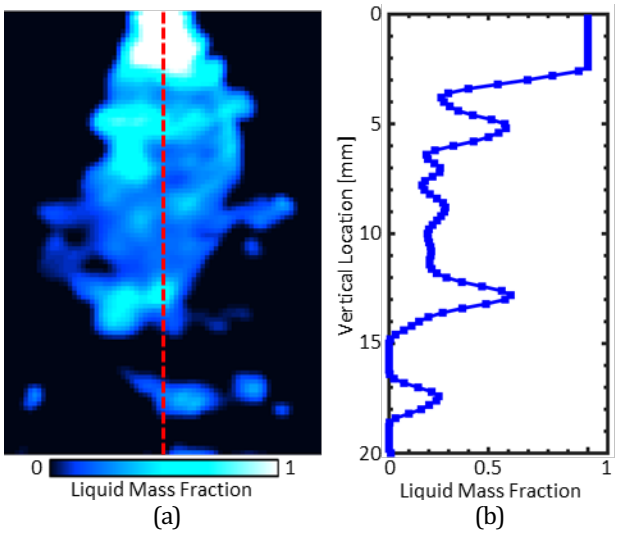

Fig. 4. (a) Planar slice at 1.2 ms through the center of the spray from the volume shown in Fig. 3, and Line plot of estimated liquid mass fraction though the center of planar slice highlighted by red dotted line.

In summary, four-dimensional measurements of liquid distribution were demonstrated in a solid cone spray using three simultaneous high-speed x-ray imaging systems. The 2D perspective data along three lines of sight were converted to an equivalent path length, and that data was used to reconstruct the time-evolving 3D volumes of liquid mass fraction. These data show the capability of the imaging system to capture the complex, four-dimensional dynamics of liquid breakup processes in multiphase flows. Future efforts include increasing the spatial resolution of the 3D volumes to more accurate represent the liquid mass fraction.

Funding. Air Force Research Laboratory (AFRL) (FA8605-15-D-2518) and the National Science Foundation (NSF) (CTS-1645544).

Acknowledgment. This manuscript has been cleared for public release by the Air Force Research Laboratory (No. 88ABW-2019-2211). SAND2019-3082 J

References

1. A. H. Lefebvre, Atomization and Sprays, (Taylor and Francis, 1989).
2. T. R. Meyer, M. Brear, S. H., Jin, and J. R. Gord, "Formation and Diagnostics of Sprays in Combustion" in Handbook of Combustion, (Wiley, New York, 2010).
3. Talley, D.G., Thamban, A.T.S., McDonell, V.G., and Samuelsen, G.S., Recent Advances in Spray Combustion: Spray Atomization and Drop Burning Phenomena (AIAA Inc., 1995).
4. V. Sick, and B. Stojkovic, Appl. Opt. **40**, 2435 (2001).
5. M. A. Linne, Prog. Energ. Combust. Sci. **39**, 403 (2013).
6. A. L. Kastengren, and C. F. Powell, Exp. Fluids, **55**, 1 (2014).
7. T. J. Heindel, At. Sprays **28**, 1029 (2018).
8. B. R. Halls, T. J. Heindel, T. R. Meyer, and A. L. Kastengren, Int. J. Multiphas. Flow **59**, 113 (2014).
9. F. Coletti, M. J. Benson, A. L. Sagues, B. H. Miller, R. Fahrig, and J. K. Eaton, J. Eng. Gas Turb. Power **136**, 051508 (2014).
10. L. Marchitto, D. Hampai, S. B. Dabagov, L. Allocca, S. Alfuso, C. Polese, and A. Liedl, Int. J. Multiphas. Flow **70**, 15 (2015).
11. J. M. Char, K. K. Kuo, and K. C. Hsieh, J. Propulsion **6**, 544 (1990).
12. A. Birk, M. McQuaid, M. Gross, Liquid core structure of evaporating sprays at high pressures – Flash X-ray Studies, Report from the Army Research Lab, Aberdeen Proving Ground-TR-901 (1995).
13. J., Lim, Y. Sivathanu, and M. Wolverton, "Evaluation of Soft X-Ray Absorption Tomography for the Near Injector Characterization of Dense Sprays," 25th ILASS-Americas (2013).
14. B. R. Halls, S. Roy, J. R. Gord, A. L. Kastengren, and T. R. Meyer, Int. J. Multiphas. Flow, **87**, 241 (2016).
15. B. R. Halls J. R. Gord, L. E. Schultz, W. C. Slowman, M.D.A. Lightfoot, S. Roy, T. R. Meyer, I. J. Multiphas. Flow **109**, 123 (2018).
16. P. J. Santangelo and P. E. Sojka, Appl. Opt. **33**, 4132 (1994).
17. J. Klinner, and C. Willert, Exp. Fluids **53**, 531 (2012).
18. E. Kristensson, E. Berrocal, and M. Aldén, Opt. Express **20**, 14437 (2012).
19. K.P. Lynch and B.S. Thurow, J. Visualization **15**, 309 (2012).
20. J. Saayman, W. Nicol, J. R. Van Ommen, R. F. Mudde, Chem. Eng. J. **234**, 437 (2013).
21. S. Moser, S. Nau, M. Salk and K. Thoma, Meas. Sci. Technol. 25, 025009 (2014).
22. M. B. Zellner, J. Perrella, D. Schall, A. Ducote, T. Nellenbach, T. O'Connor, T. Quigg, N. Sturgill, TR AD1058059, 01 Oct 2017,31 Jul 2018.
23. T. R. Meyer, B. R. Halls, N. Jiang, M. N. Slipchenko, S. Roy, and J. R. Gord, Opt. Express **24**, 29547 (2016).
24. B. R. Halls, P. S. Hsu, N. Jiang, E. S. Legge, J. J. Felver, M. N. Slipchenko, S. Roy, T. R. Meyer, and J. R. Gord, Optica **4**, 897 (2017).
25. G.E. Elsinga, F. Scarano, B. Wieneke and B.W. van Oudheusden, Exp. Fluids **41**, 933 (2006).
26. Y. Wu, Q. Lei, and L. Ma, Appl. Opt. **53**, 5547 (2014).
27. N. Rahman, B. R. Halls, J. W. James, A. McMaster, M. D. A. Lightfoot, J. R. Gord, and T. R. Meyer, 4D Imaging of Primary Liquid Breakup using High-Speed Tomographic X-Ray Radiography, ICLASS 2018, 14th Triennial Int. Conf. on Liquid Atomization and Spray Systems, Chicago, IL, July 22–26, 2018.
28. M. Sanchez del Rio and R. J. Dejus, "Status of XOP: v2.4: recent developments of the x-ray optics software toolkit," SPIE Proc., 814115 (2011).
29. J. Floyd, P. Geipel, A. M. Kempf, Combust. Flame **158**, 376 (2011).

References with Full Citations

1. Lefebvre, A. H., Atomization and Sprays, (Taylor and Francis, 1989).
2. T. R. Meyer, M. Brear, S. H., Jin, and J. R. Gord, "Formation and Diagnostics of Sprays in Combustion" in Handbook of Combustion, (Wiley, New York, 2010).
3. Talley, D.G., Thamban, A.T.S., McDonell, V.G., and Samuelsen, G.S., "Laser sheet visualization of spray structure," Recent Advances in Spray Combustion: Spray Atomization and Drop Burning Phenomena (AIAA Inc., 1995).
4. Sick, V. and Stojkovic, B., "Attenuation effects on imaging diagnostics of hollow-cone sprays," Appl. Opt. 40(15), pp. 2435–2442 (2001).
5. M. A. Linne, "Imaging in the Optically Dense Regions of a Spray: A Review of Developing Techniques," Prog. Energ. Combust. Sci. 39, 403–440 (2013).
6. Kastengren, A.L., and Powell, C.F., "Synchrotron X-ray techniques for fluid dynamics," Exp. Fluids, 55(3), pp. 1–15 (2014).
7. T. J. Heindel, "X-ray Imagng Techniques to Quantify Spray Characteristics in the Near Field," At. Sprays 28, 1029 (2018).
8. B. R. Halls, T. J. Heindel, T. R. Meyer, and A. L. Kastengren, "Evaluation of X-ray sources for quantitative two- and three-dimensional imaging of liquid mass distribution in atomizing sprays," Int. J. Multiphas. Flow 59, 113–120 (2014).
9. F. Coletti, M. J. Benson, A. L. Sagues, B. H. Miller, R. Fahrig, and J. K. Eaton, "Three-Dimensional Mass Fraction Distribution of a Spray Measured by X-Ray Computed Tomography," J. Eng. Gas Turb. Power 136(5), 051508 (2014).
10. L. Marchitto, D. Hampai, S. B. Dabagov, L. Allocca, S. Alfuso, C. Polese, and A. Liedl, "GDI spray structure analysis by polycapillary X-ray μ-tomography, Int. J. Multiphas Flow 70, 15–21 (2015).
11. J. M. Char, K. K. Kuo, and K. C. Hsieh, "Observations of Breakup Processes of Liquid Jets Using Real-Time X-ray Radiography," J. Propulsion 6, 544–551 (1990).
12. Birk, A., McQuaid, M., Gross, M., 1995. Liquid core structure of evaporating sprays at high pressures – Flash X-ray Studies, Report from the Army Research Lab, Aberdeen Proving Ground-TR-901 (1995).
13. J., Lim, Y. Sivathanu, and M. Wolverton, "Evaluation of Soft X-Ray Absorption Tomography for the Near Injector Characterization of Dense Sprays," 25th ILASS-Americas, (2013).
14. B. R. Halls, S. Roy, J. R. Gord, A. L. Kastengren, and T. R. Meyer, Quantitative imaging of time-resolved liquid distributions in sprays using broadband flash x-ray radiography, Int. J. Multiphase Flow, 87, 241 (2016).
15. B. R. Halls J. R. Gord, L. E. Schultz, W. C. Slowman, M.D.A. Lightfoot, S. Roy, T. R. Meyer, "Quantitative 10–50 kHz X-ray Radiography of Liquid Spray Distributions Using a Rotating-Anode Tube Source," I. J. Multiphas. Flow 109, 123 (2018).
16. P. J. Santangelo and P. E. Sojka, "Focused-image holography as a dense-spray diagnostic," Appl. Opt. 33, 4132–4136 (1994).
17. J. Klinner, and C. Willert, "Tomographic shadowgraphy for three-dimensional reconstruction of instantaneous spray distributions," Exp. Fluids 53, 531–543 (2012).
18. E. Kristensson, E. Berrocal, and M. Aldén, "Quantitative 3D imaging of scattering media using structured illumination and computed tomography," Opt. Express 20, 14437–14450 (2012).
19. K.P. Lynch and B.S. Thurow, "3-D flow visualization of axisymmetric jets at Reynolds number 6,700 and 10,200," J. Visualization 15 (4) (2012) 309-319.
20. J. Saayman, W. Nicol, J. R. Van Ommen, R. F. Mudde, "Fast X-Ray Tomography for the Quantification of the Bubbling-, Turbulent-, and Fast Fluidization-Flow Regimes and Void Structures," Chem. Eng. J. 234, 437 (2013).
21. S. Moser, S. Nau, M. Salk and K. Thoma, "In situ flash x-ray high-speed computed tomography for the quantitative analysis of highly dynamic processes," Meas. Sci. Technol. 25, 025009 (2014).
22. M. B. Zellner, J. Perrella, D. Schall, A. Ducote, T. Nellenbach, T. O'Connor, T. Quigg, N. Sturgill, "Assessing X ray Contamination from Neighboring Sources in the US Army Research Laboratory's (ARL's) Multi Energy Flash Computed Tomography Diagnostic," Technical Report,01 Oct 2017,31 Jul 2018.
23. T. R. Meyer, B. R. Halls, N. Jiang, M. N. Slipchenko, S. Roy, and J. R. Gord, "High-Speed, Three-Dimensional Tomographic Laser-Induced Incandescence Imaging of Soot Volume Fraction in Turbulent Flames," Opt. Express 24, 29547–29555 (2016).
24. B. R. Halls, P. S. Hsu, N. Jiang, E. S. Legge, J. J. Felver, M. N. Slipchenko, S. Roy, T. R. Meyer, and J. R. Gord, "kHz-rate four-dimensional fluorescence tomography using an ultraviolet-tunable narrowband burst-mode optical parametric oscillator," Optica 4(8) 897–902 (2017).
25. G.E. Elsinga, F. Scarano, B. Wieneke and B.W. van Oudheusden, "Tomographic particle image velocimetry," Exp. Fluids 41 (6) (2006) 933-947.
26. Wu, Y., Q. Lei, and L. Ma, "Experimental demonstration of 4D imaging in two-phase flows based on computed tomography at 5 kHz," Applied Optics 53, 5547-5553 (2014).
27. N. Rahman, B. R. Halls, J. W. James, A. McMaster, M. D. A. Lightfoot, J. R. Gord, and T. R. Meyer, 4D Imaging of Primary Liquid Breakup using High-Speed Tomographic X-Ray Radiography, ICLASS 2018, 14th Triennial Int. Conf. on Liquid Atomization and Spray Systems, Chicago, IL, July 22–26, 2018.
28. M. Sanchez del Rio and R. J. Dejus, "Status of XOP: v2.4: recent developments of the x-ray optics software toolkit," SPIE Proc., 814115 (2011).
29. J. Floyd, P. Geipel, A. M. Kempf, "Computed Tomography of Chemiluminescence (CTC): Instantaneous 3D Measurements and Phantom Studies of a Turbulent Opposed Jet Flame," Combust. Flame 158, 376–391 (2011).